Plasmonic hybridization properties in polyenes octatetraene molecules based on theoretical computation

Nan Gao(高楠)[1], Guodong Zhu(朱国栋)[1], Yingzhou Huang(黄映洲)[2], and Yurui Fang(方蔚瑞)[1,†]

[1] *Key Laboratory of Materials Modification by Laser, Electron, and Ion Beams (Ministry of Education), and School of Physics, Dalian University of Technology, Dalian* 116024, *China*

[2] *State Key Laboratory of Coal Mine Disaster Dynamics and Control, Chongqing University, Chongqing* 400044, *China*

(Received 29 June 2022; revised manuscript received 22 July 2022; accepted manuscript online 12 August 2022)

Relationship of plasmonic properties of multiple clusters to molecular interactions and properties of a single cluster or molecule have become increasingly important due to the continuous emergence of molecular and cluster devices or systems. A hybrid phenomenon similar to plasmonic nanoparticle hybridization exists between two molecules with plasmon excitation modes. We use linear-response time-dependent density functional theory, real-time propagation time-dependent density functional theory, the plasmonicity index, and transition contribution maps (TCMs) to identify the plasmon excitation modes for the linear polyenes octatetraene with –OH and $–NH_2$ groups and analyze the hybridization characteristics using charge transitions. The results show that molecular plasmon hybridization exists when the two molecules are coupled. The TCM analysis shows that the plasmon modes and hybridization result from collective and single-particle excitation. The plasmon mode is stronger, and the individual properties of the molecules are maintained after coupling when there is extra charge depose in the molecules because the electrons are moving in the molecules. This study provides new insights into the molecular plasmon hybridization of coupled molecules.

Keywords: plasmon hybridization, molecular plasmon, time-dependent density functional theory (TDDFT)

PACS: 71.45.Gm, 73.20.Mf, 31.15.ae, 31.15.A– **DOI:** 10.1088/1674-1056/ac891c

1. Introduction

Plasmons arise from the long-range Coulomb interaction between electrons. It can be regarded as a quantized charge density wave and exhibits collective electronic oscillations on metal nanostructures, providing an effective mechanism for sub-wavelength light confinement and manipulation.[1] In recent years, plasmon excitation in molecular-level systems has been widely investigated, such as plasmon catalysis,[2–4] quantum plasmons,[5,6] and strong plasmon–molecule coupling.[7] The classical electromagnetic theory cannot adequately describe the properties of plasmons because of the size limitation; instead, quantum mechanics (QM) is required. The concept of molecular plasmon excitation is analogous to plasmon oscillation in metal structures, which recognizes the collective electronic excitation behavior similar to plasmon characteristics as molecular plasmon excitation.[8,9] Research of molecular plasmons will extend the unique properties of plasmons at the microscopic scale.[10,11] Obvious plasmon excitation modes have been observed in sodium,[12] gold and silver chains and clusters,[10,11,13,14] octatetraene chains,[15,16] polycyclic aromatic hydrocarbons (PAHs),[14,17–20] graphene,[21] and other compounds. Properties of molecular plasmons have implications in many fields, including sensing,[22–26] optoelectronics,[18,19,27–29] and optical nanocircuits.[30] It is expected that the optical resolution will reach the molecular scale.

Due to the continuous emergence of molecular and cluster devices and systems, investigating molecular plasmon excitation and the coupling properties has become increasingly important. Several research groups are currently investigating molecular/cluster plasmons identifying their properties.[13–16,20] However, when many molecules and clusters form a multi-molecular ensemble, the coupling makes it difficult to assess plasmon excitation, especially when a charge transfer or bond exists between the molecules or a new molecule is formed. Therefore, relationship between plasmonic properties of multiple clusters and molecular interactions of individual clusters or molecules remains unclear. Based on the concept of strong plasmon coupling,[31–33] Rossi *et al.* used the cavity quantum electrodynamic density functional theory (cQED-DFT) to analyze plasmon coupling between aluminum clusters and benzene rings. As the number of benzene rings increases, the coupling phenomenon would become more pronounced.[7] The phenomenon of strong coupling characteristic of plasmons also exists in small molecule and cluster systems and is referred to as molecular plasmon hybridization (MPH) here. When analogizing to plasmon hybridization of particles,[34] it is unclear whether hybridization occurs between two molecules with plasmon excitation modes. In response to this question, characteristics of plasmon excitation modes and charge transition in both individual and assembled molecules are analyzed in small molecular chains. The plasmonicity index (PI)[14,20] has been used to identify the molecular plasmon excitation mode of molecu-

†Corresponding author. E-mail: yrfang@dlut.edu.cn

© 2023 Chinese Physical Society and IOP Publishing Ltd

lar systems (including single-particle excitation and plasmon excitation with electron–electron interaction). The electron excitation is typically complex in small-sized plasmon systems (single molecules or small clusters), and an effective method is required to distinguish the excitation of single electrons and plasmons for a chain octatetraene system.[13–16] Gil-Guerrero *et al.* proposed electron density descriptors to identify molecular plasmons.[35] This method utilizes the electron density related to electronic excitation instead of the excitation energy. The authors analyzed the eigenvalues of the differential density matrix obtained by the time-dependent density functional theory (TDDFT) and time-dependent Hartree–Fock (TDHF) theory to investigate plasmonic excitation. Their method of identifying molecular plasmons avoids adoption non-interacting electronic models as a reference for single-electron excitation in molecular mechanisms with discrete orbital energy distributions. Different scaling produced multiple calculations are also not required. In addition, the time-related calculation framework was adopted to determine the system response to electromagnetic radiation, which is particularly important in small systems. Therefore, TDDFT has been used to analyze the hybrid properties of two neutral chain molecular systems in this paper. TDDFT usually has two forms: real-time TDDFT (RT-TDDFT) and linear response TDDFT (LR-TDDFT). Both forms can be used to obtain the Kohn–Sham (KS) electron–hole transition terms to analyze the electronic excitation. In the real-time propagation framework, the electron–hole contribution provides detailed information on the QM to understand plasmon absorption. It can be visualized in two-dimensional (2D) transition contribution maps (TCMs).[8] Through the phenomenon of the energy level corresponding to the plasmon mode splits, the plasmon properties of two linked molecules can be explained by the plasmon hybridization theory. In addition, an increase or decrease in the charge can be used to control MPH.[17–19] Therefore, we analyze whether an increase or decrease exists in the charge affects plasmon hybridization. In-depth research on MPH can provide information of hybridization properties at molecular level.

We use the following approach to analyze MPH. We identify the plasmonic mode of octatetraeneamine ($C_8H_9NH_2$) and octateraenealcohol (C_8H_9OH) using a finite one-dimensional (1D) electron gas model. Subsequently, we analyze the hybridization phenomenon and the internal mechanism of two hybrid molecule configurations using the PI and the TDDFT. We then demonstrate the ability to tune MPH.

The system we investigate is shown in Fig. 1. We selected octatetraene as the initial structure because the carbon atom chain exhibits plasmon excitation.[16] In plasmon hybridization research it is better to have the two objects whose plasmon characteristics should be distinguishable. Therefore, we added different electron-donating groups (–OH and $–NH_2$) at one end of octatetraene. In addition, we selected two coupling configurations: head-to-tail (HT) and head-to-head (HH).

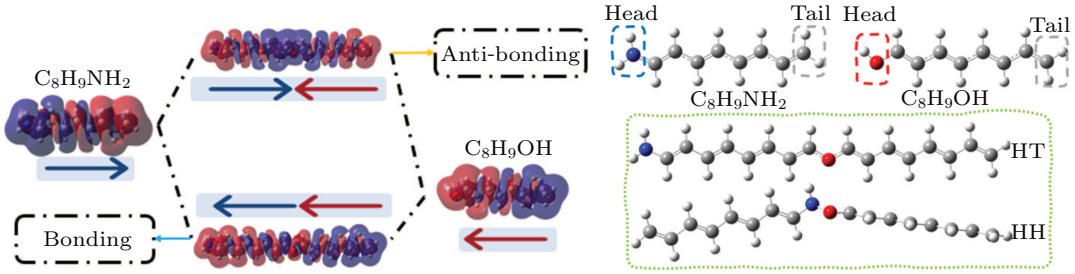


Fig. 1. The schematic diagram of plasmon hybridization (left panel). The right panel shows the initial structure ($C_8H_9NH_2$ and C_8H_9OH) and hybrid structure of the HT and HH configurations.

2. Simulation methods

2.1. LR-TDDFT calculations

The main skeleton part of the initial structure (i.e., the octatetraene) was based on the previous studies.[15,16] The theoretical calculations of quantum chemistry were conducted in the Gaussian 16 software package.[36] The B3LYP/6-311G(d,p) basis sets[37] were used for the DFT calculation[38] of the geometric optimization and ground-state calculation of the $C_8H_9NH_2$ and C_8H_9OH. The ground-state geometric optimization and related vibration frequency based on the same level calculation provided the minimum value of the optimum potential energy surface, and no virtual frequency was observed. In order to achieve a high photoabsorption spectrum matching between the LR-TDDFT and RT-TDDFT, we tested different functional and basis sets aiming to select the best method, see the relevant statement in the supporting information (see supplementary Notes S1 and Fig. S1). Therefore, The LR-TDDFT photoabsorption spectrum was performed using the PBE0/6-311G(d,p) basis sets.[39] In addition, all the orbital transition contributions greater or equal to 10^{-5} to each excitation state are considered to ensure an accurate description of the excitation state. For charge-doped systems, we added an additional negative charge in the $C_8H_9NH_2^-$ and $C_8H_9OH^-$ structures, while in the HT^{2-} and HH^{2-} configurations, we added two charges to balance the coupling effect. The calculation method is the same as that of neutral molecules.

In the time-dependent framework (TDDFT and TDHF),

the relationship between electronic excitation/deexcitation and the collective transition can be established using virtual electrons. Therefore, the total number of electrons promoted from the ground state (0) to the excited state (I) can be expressed as $N^{0\to \mathrm{I}} = \sum_{i=N_{\mathrm{occ}}+1}^{N_{\mathrm{T}}} \sum_{a=1}^{N_{\mathrm{occ}}} \left(X_{ai}^{\mathrm{I}*} X_{ai}^{\mathrm{I}} + Y_{ai}^{\mathrm{I}} Y_{ai}^{\mathrm{I}*} \right)$, where N_{T} represents the total number of orbitals, N_{occ} represents the number of occupied orbitals, X_{ai}^{I} and Y_{ai}^{I} represent the excitation and deexcitation coefficients, respectively. Due to the normalization of the wave function, the sum of the squares of all possible excitation coefficients associated with single-electron excitation equals one. The equation also includes deexcitation terms closely related to the collective excitation (between 0 and 1). The larger the contribution of the Y_{ai}^{I} coefficient, the greater the deviation of $N^{0\to \mathrm{I}}$ is from the reference value (1.0) (i.e., the deviation from the single-electron excitation). Thus, we use the logarithmic function to define the PI as

$$\delta = 10^{N^{0\to \mathrm{I}}-1}. \tag{1}$$

In addition, according to the transition density matrix for an excitation I obtained from TDDFT (or TDHF), we calculate the corresponding transition density

$$\rho^{\mathrm{I}}(\boldsymbol{r}) = \sum_{a=1}^{N_{\mathrm{occ}}} \sum_{i=N_{\mathrm{occ}}+1}^{N_{\mathrm{T}}} X_{ai}^{\mathrm{I}} \phi_a^*(\boldsymbol{r}) \phi_i(\boldsymbol{r}) + Y_{ai}^{\mathrm{I}} \phi_a(\boldsymbol{r}) \phi_i^*(\boldsymbol{r}). \tag{2}$$

2.2. RT-TDDFT calculations

Furthermore, the optical properties under the RT-TDDFT framework are considered, the DFT and TDDFT calculations were carried out using the Perdew–Burke–Ernzerhof (PBE)[40] exchange–correlation functional in the adiabatic limit. The photoabsorption spectra are calculated using the δ-kick technique[41] in the linear-response regime and employing the dipole approximation for light–matter interaction. The spectrum is presented as the dipole strength function that is equivalent to photoabsorption cross section apart from a constant multiplier. The default projector augmented-wave (PAW)[42] data sets and double-ζ polarized (dzp) basis sets provided in GPAW were used for C, N, O, and H. The dzp basis set are important for describing plasmon resonances.[43] In general, while the used basis sets might not be adequate for yielding numerical values at the complete-basis-set limit, they are expected to be sufficient for the purposes of the present work. For real-time TDDFT a grid spacing parameter of 0.3 Å was chosen to represent densities and potentials, and the molecules were surrounded by a vacuum region of at least 6 Å. For the time propagation, we used a time step of $\Delta t = 20$ as (attosecond) and total propagation time of at least $T = 30$ fs. The spectra were broadened using Lorentzian spectral broadening with 0.3 eV corresponding to a full width at half-maximum of 0.6 eV. The DFT calculations were carried out using the GPAW (version: 21.6.0) package[44,45] with localized basis sets (LCAO mode)[46] and with uniform real-space grids with the finite difference approximation. TDDFT calculations were conducted using the LCAO-RT-TDDFT implementation in GPAW.[47] The ASE library[48] was used for constructing the atomic structures. The NumPy,[49] SciPy,[50] and Matplotlib,[51] Python packages were used for processing data and generating figures.

3. Results and discussion

3.1. Plasmonic properties analysis

We compared the excitation modes obtained from the TDDFT and the dispersion curve of the quantum mechanism to distinguish the plasmon excitation and single-electron excitation of the molecular chain to obtain the molecular plasmon excitation modes. The minutiae of 1D finite electron gas model for the plasmon dispersion relationship are given in supplementary Note S2. The area surrounded by the red lines in Fig. S2 indicates the single-particle excitation in the 1D finite uniform electron gas model; and the electron excitation in this area is independent of the Coulomb interaction. Figure S2(a) shows that the plasmon excitation (blue solid dots) can be distinguished from the single-particle excitation. In addition, the excitation modes obtained from the TDDFT show that the collective excitation modes with lower energy (P1 and the corresponding plasmon index can be found in Table S1, excitation is 4.04 eV and main electron transition is $S_0 \to S_1$) match the plasmon excitation in the electron gas model. The upper panel in Fig. 2(a) shows the transition density isosurfaces of the two lower plasmon excitation modes; red corresponds to the positive phase and blue corresponds to the negative phase. The transition density of the plasmon has an envelope explanation is that the plasmon, as a collective electron excitation, exhibits standing wave density, which is observed in the transition density. The other oscillations are caused by the finite size. Similarly, $C_8H_9NH_2$ also has a low-energy plasmon excitation modes [see Fig. 2(b)], which agrees with the 1D finite plasmon excitation model (see Fig. S2 from supporting information). The upper panel in Fig. 2(b) shows the isosurface of the transition density of $C_8H_9NH_2$ and the excitation modes are similar to C_8H_9OH, except that the vibration direction is opposite.

In addition, the LR-TDDFT and RT-TDDFT were used to analyze the electronic excitations of both octatetraene chain molecules. As shown in Fig. 2(a), the absorption spectra obtained from the two theoretical methods have a large absorption peak around 3.9 eV, there has a slight blue shift of the optical absorption peak obtained from the LR-TDDFT relative to RT-TDDFT. The plasmon excitation mode P1 (the corresponding plasmon index can be found in Table S1) of

C_8H_9OH corresponding to the linear response method is located at 4.04 eV, which is in good agreement with the induced density obtained from the real-space method (3.88 eV) (yellow corresponds to the positive phase, and cyan corresponds to the negative phase). Figure 2(b) shows the photoabsorption spectrum of $C_8H_9NH_2$. The induced density obtained from the real-space method at the resonance energy of 3.70 eV is in good agreement with the transition density obtained from the linear response, demonstrating that though there is a difference between the maximum absorption peak positions obtained with the two methods, it is the same excitation peak.

The TCM is useful to analyze the response of the KS electron–hole transition contributions to the photoabsorption and represents the plasmon properties. The resonance is typically a superposition of many electron–hole excitations. In TCM, the photoabsorption cross section $S(\omega)$ is expressed in the basis of occupied (i) and unoccupied (a) KS states as $S(\omega) = \sum_{ia} S_{ia}(\omega)$, and the elements of the matrix $S_{ia}(\omega)$ are plotted at selected resonance energies on a Gaussian broadened two-dimensional plane spanned by the energy axes for occupied and unoccupied KS states.[7–9,52,53] Figure 2(c) shows the TCM and the density of states (DOS) of C_8H_9OH at resonance energies, where red and blue represent the positive and negative values, respectively, of the photoabsorption decomposition in the x-direction. Due to the small molecular size, the C_8H_9OH molecule has well-separated discrete KS states, which is confirmed by the DOS diagrams. The TCM of the C_8H_9OH molecule maximum absorption peak corresponding to the resonance energy ($\omega = 3.88$ eV) shows a strong positive contribution (s-electron transition) in the region below the resonance energy. The low-energy transition that forms this plasmon excitation remains essentially constant within the frequency window as the energy changes. The TCM corresponding to the main resonant frequency of $C_8H_9NH_2$ is shown in Fig. 2(d), indicating a stronger positive contribution at resonant energies of $\omega = 3.70$ eV, which is due to s-electron transition. Small-molecule plasmon excitation results from the coupling between the positive contribution of the collective oscillations and the single KS transition. In summary, both molecules have a lower-energy plasmon excitation mode, and the excitation mode is strongly related to the global charge transition.

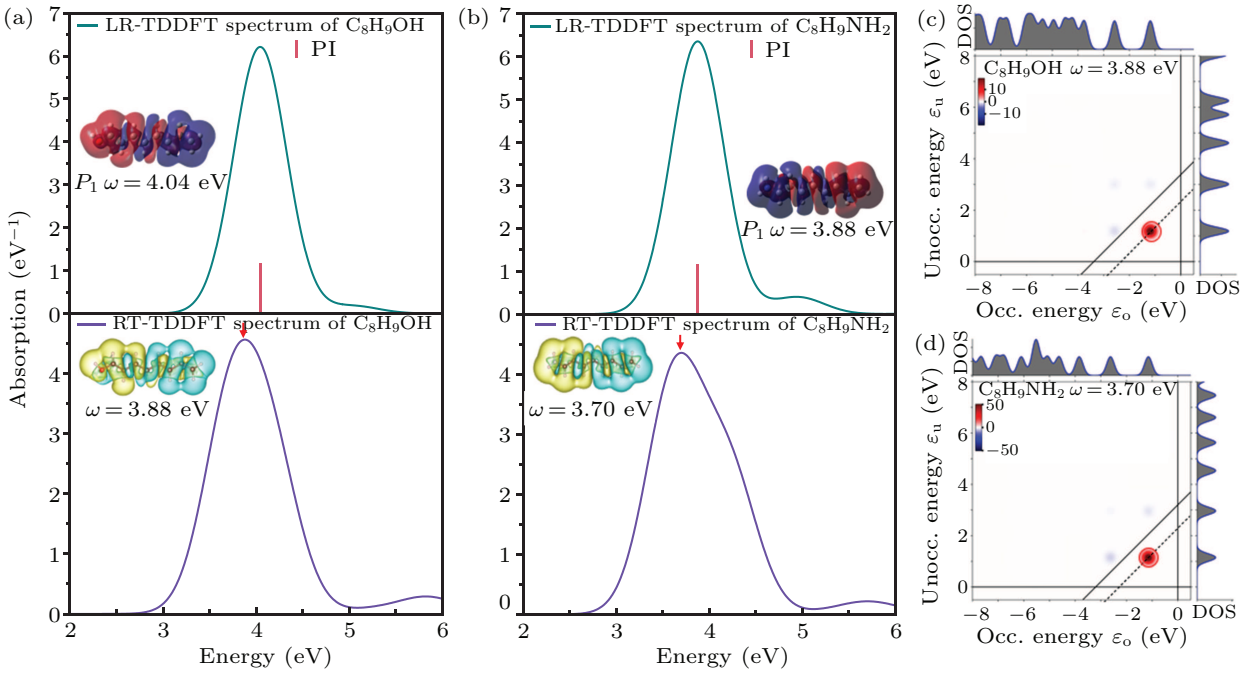


Fig. 2. The LR-TDDFT (upper) and RT-TDDFT (lower) absorption spectra of (a) C_8H_9OH and (b) $C_8H_9NH_2$. The transition densities corresponding to the plasmon excitation modes are also depicted in the upper panel, and the induced charge density contribution is shown in the lower panel. The transition contribution maps (TCMs) of (c) C_8H_9OH and (d) $C_8H_9NH_2$ corresponding to the main resonance energies ω calculated by the RT-TDDFT method, where red and blue indicate positive and negative contributions, respectively. The solid line is the constant for transition energy ($\varepsilon_u - \varepsilon_o = \omega$).

3.2. Molecular hybridization analysis

When the two types of octatetraene molecules form a chain, new molecular plasmon modes occur during excitation. In the following, we discuss the molecular plasmon modes from hybridization point of view for two neutral hybrid configurations (HT and HH). Traditional plasmon hybridization studies based on the hydro electrodynamics theory consider that the plasmon interactions of the hybrid system cause a plasmon energy shift and the mixing or hybridization between two free plasmon modes (i.e., spherical and cavity plasma).[34] The hybridization depends on the strength of the interaction and the energy of the original plasmon modes.

The coupling and blending of the modes produce the unique tunability of the metal nanoshells. No charge transfer occurs between the two objects during plasmon hybridization, and only energy is exchanged. However, a charge transfer occurs in small-molecule systems, and new bonds form between the two molecules. Thus, the quantum chemical method other than the electromagnetic method is used here. As shown in Fig. 3(a), the HT configuration shows a strong absorption peak in the low-energy region. One plasmon excitation mode with a strong absorption peak in the low-energy region is observed for the $C_8H_9NH_2$ or C_8H_9OH molecules. However, the HT configuration has more than one plasmon mode in the low-energy region. Here we only consider the excitation modes with a relatively large PI. We assume that a PI close to 1 indicates a single-particle excitation and ignore it. In the HT configuration, the mode of the hybrid molecule splits into three excitation modes (the corresponding plasmon index can be found in Table S1) in contrast to the P1 mode of two single molecules [see the energy level splitting diagram in Fig. S6(a)]. The high-energy mode iii for HT configuration (4.11 eV, $S_0 \rightarrow S_3$) corresponds to symmetric coupling (anti-bonding), and the low-energy mode i (2.94 eV, $S_0 \rightarrow S_1$) and ii (3.50 eV, $S_0 \rightarrow S_2$) corresponds to antisymmetric coupling (bonding). In addition, the RT-TDDFT spectrum shows that the induced charge density of the excitation mode at the maximum absorption peak (2.79 eV and 3.35 eV) shows plasmon bonding modes [upper panel in Fig. 3(c)] and matches the i and ii modes obtained by LR-TDDFT, respectively, showing a high degree of consistency. At the same time, the induced charge density located in the RT-TDDFT spectrum with resonance energy of 4.05 eV has a good agreement with the linear response mode iii (both anti-bonding modes). The charge density distributions in the inset show that this is a hybridization manner for the new plasmon modes. The resonance energy in the coupling system is the same as that in traditional hybridization. A similar hybrid behavior is observed for the HH configurations [lower panel in Fig. 3(b), and Fig. S3]. Unlike in the HT configuration, the charge transition has changed substantially in the hybridization of the plasmon excitation modes [see lower panel in Fig. 3(b), and i, ii and iii modes in Fig. S3] for the HH configuration due to the formation of an angle when the two initial molecules are hybridized. Note that the $C_8H_9NH_2$ molecule is inverted in the HH configuration relative to the HT configuration (see Fig. 1). The high-energy mode iii for HH configuration (4.17 eV, $S_0 \rightarrow S_4$) corresponds to symmetric coupling (anti-bonding), and the low-energy mode i (3.59 eV, $S_0 \rightarrow S_2$) and ii (3.80 eV, $S_0 \rightarrow S_3$) corresponds to antisymmetric coupling (bonding), and the bonding and anti-bonding can be clearly seen from the phase at the junction of the two initial molecules of the transition density map [also see the energy level splitting diagram in Fig. S6(b)]. Similarly, in the HH configuration RT-TDDFT spectrum at the resonance energies of 3.35 eV and 3.88 eV [lower panel in Fig. 3(c)] the induced charge density shows good agreement with the transition density of the linear response i and ii modes indicating that the plasmonic mode can splits into two similar plasmonic bonding modes in the low-energy region after hybrid, which is just opposite to the HT configuration, the HT splits into two opposite plasmonic bonding modes after hybrid (opposite dipoles resonance). In addition, the induced charge density corresponding to the high-energy plasmonic mode ($\omega = 4.25$ eV) of real time also shows a high consistency with the iii mode of linear response (anti-bonding mode). The above discussion proves the fact that plasmon modes can split after hybridization and confirms the collective oscillations of the plasmon modes.

The TCMs of the photoabsorption spectrum of the HT and HH configurations are shown in Fig. 4. Figures 4(a)–4(d) show that the HT configuration has more electron–hole contributions to the resonance energy, unlike the more discrete KS contribution of the single molecule. The HT configuration shows a more concentrated positive contribution to the resonance energy at the highest absorption peak ($\omega = 2.79$ eV). The concentrated and strong positive contribution below the resonance energy region is important for plasmon excitations, whereas the negative contribution above the resonance energy region may be attributed to the sp electron transition during the plasmon oscillation. It is worth noting that the resonance energy is a negative contribution at 2.79 eV to be reversed to a positive contribution at 3.35 eV, which should be the result of the charge transition. As the resonance energy increases, some high-energy electron transitions located near the resonance energy (solid black line) are contributing additionally to the plasmon excitation in the modes with higher plasmon resonance energies ($\omega = 4.05$ eV and $\omega = 4.19$ eV), at the same time, the positive contribution below the resonant energy region is reversed to a negative contribution due to the charge transition (dashed red ellipse). This response may be attributed to the coupling between the positive contribution corresponding to the plasmon and the single-electron transition, i.e., the splitting of the plasmon mode into multiple resonances, forming an antisymmetric and symmetric combination with KS transition and plasmon transition. In large-scale systems, the interaction between plasmons and the nearby KS transitions is very weak, and the coupling is regarded as a broadening peak of the plasmon excitation. Figures 4(e)–4(g) show that the HH configuration has few and dispersed KS contributions. As the resonance energy increases, the weakening of the strength of the positive contribution is accompanied by the appearance of negative contributions (dashed black circles). The charge transfer may be the key to the transition between bonding and

anti-bonding modes. Compared to the HT configuration, no significant changes occur in the positive and negative contributions as the frequency changes, which would lead to weaker hybridization properties in the HH configuration than in the HT configuration. This result may be due to the different relative positions of the two different electron-donating groups in the molecular chain. In the HT configuration, the O atom in the middle of the molecule provides a bridge for the intramolecular charge transfer, resulting in strong hybridization. In contrast, in the HH configuration, both electron-donating groups are located in the middle of the molecular chain. Thus, a local charge transfer occurs in the molecular chain, which may be responsible for the few and dispersed KS contributions. In general, the HT configuration produces a strong directional intramolecular charge transfer due to the unique arrangement of the electron-donating groups, resulting in a strong concentrated KS electron–hole contribution and a split of the plasmon mode into multiple modes. In contrast, the intramolecular charge transfer is relatively weak in the HH configuration and is accompanied by local electron transfer, leading to the plasmon hybridization weaker than those in the other two configurations.

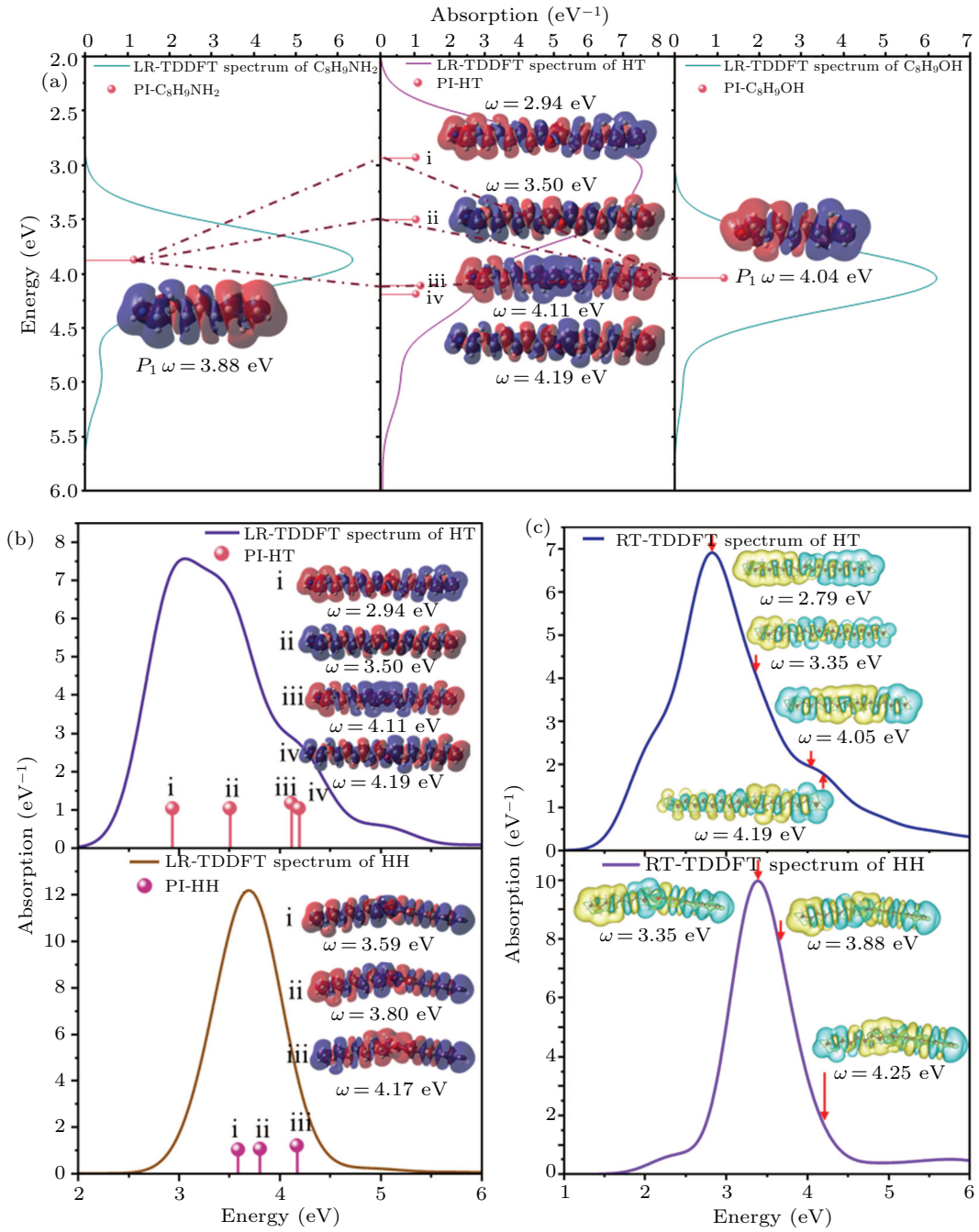


Fig. 3. Schematic diagram of plasmon hybridization for the HT and HH configurations: (a) the hybridization and energy split of the HT configuration, (b) the LR-TDDFT photoabsorption spectrum for the HT and HH configurations (curves) and the transition density isosurface of the main excitations modes (the vertical red line indicates the plasmonicity index), (c) the RT-TDDFT photoabsorption spectrum for the HT and HH configurations (curves). The main resonances are shown as induced charge density isosurfaces.

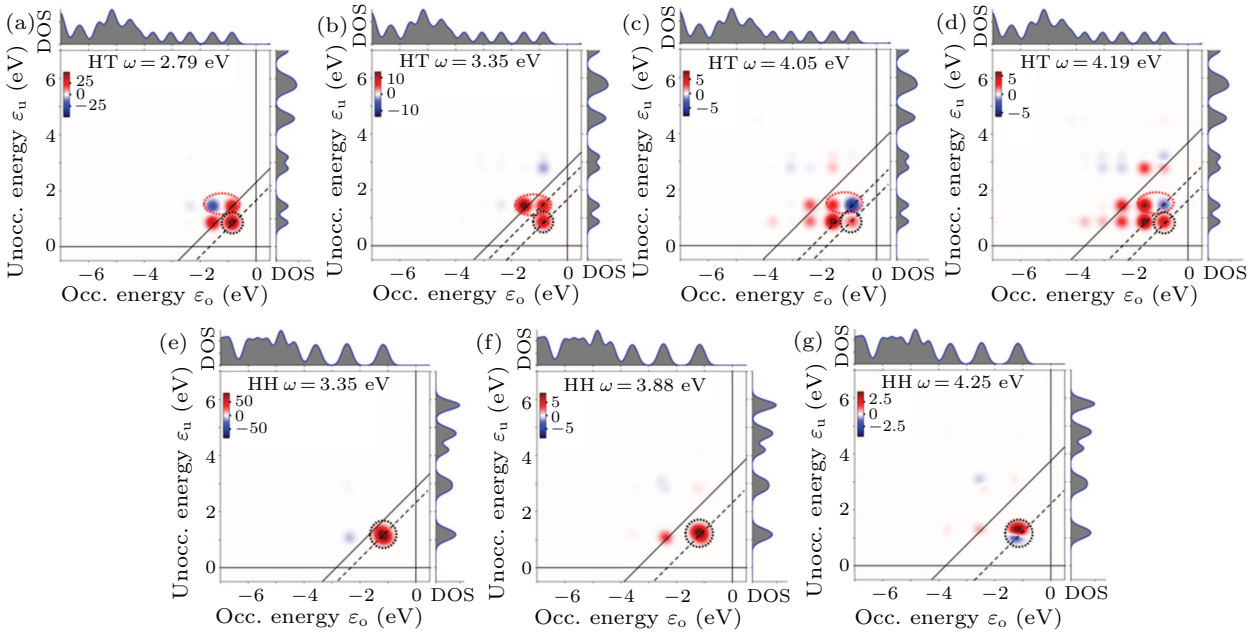


Fig. 4. The TCMs of the photoabsorption decomposition of the HT configuration [(a)–(d)] and HH configuration [(e)–(g)] at different resonance energies ω. The solid line is the constant for transition energy ($\varepsilon_u - \varepsilon_o = \omega$).

3.3. Tunability of molecular plasmon hybridization

The plasmons of small-molecule systems can be tuned by charge doping.[17] We systematically analyzed the effects of negative charge doping on plasmon excitation of hybrid systems. Figure 5 shows the photoabsorption spectrum and induced density of the charge doped $C_8H_9NH_2^-$ and $C_8H_9OH^-$. As shown in Fig. 5(a), the results of the linear response analysis show a broad absorption peak in the low-energy region of $C_8H_9OH^-$. However, there are two excitations that have a PI, and the PI does not exceed 2 (see Table S2), because of the short chain of the octatetraene molecule. Similar to neutral molecules (see Fig. 2), we identify relatively large i modes as plasmonic excited modes. Furthermore, the absorption spectra obtained from the real-space method indicate a good agreement with the linear response. The induced density at the linear response energy of 3.28 eV shows a good agreement (opposite positive and negative phases) with the induced density at the resonance energy of 3.77 eV in the real space. The plasmon response of $C_8H_9NH_2^-$ is highly similar, as shown in Fig. 5(b).

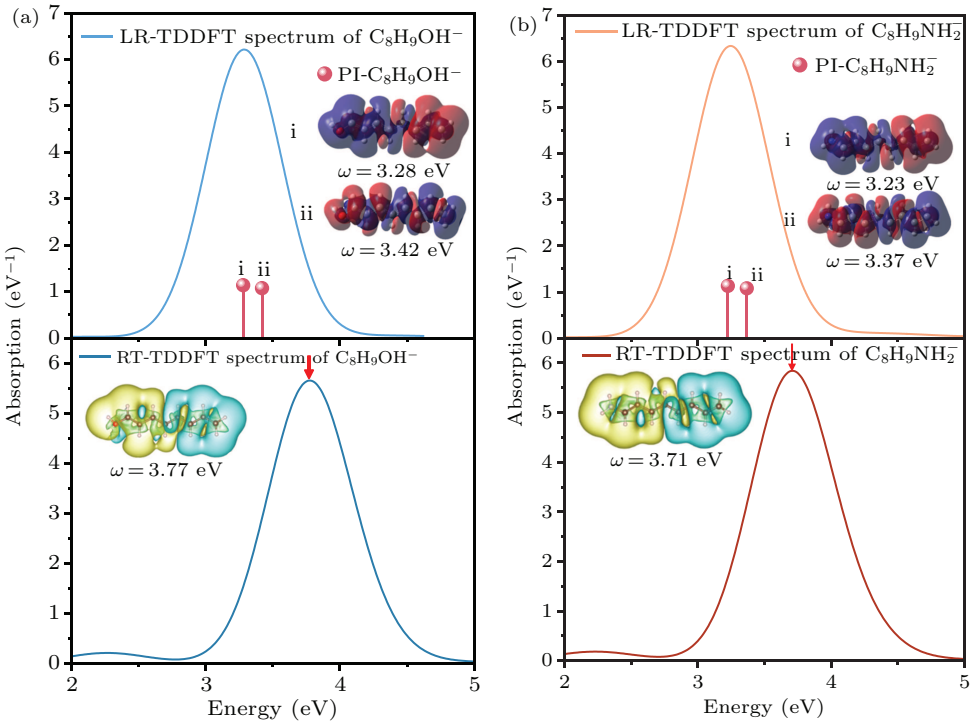


Fig. 5. (a) The LR-TDDFT (upper) and RT-TDDFT (lower) photoabsorption spectrum of $C_8H_9OH^-$. (b) The LR-TDDFT (upper) and RT-TDDFT (lower) photoabsorption spectrum of $C_8H_9NH_2^-$, where transition density isosurfaces of the main excitation modes are drawn in upper panel and the induced charge density contribution are plotted in lower panel.

The TCMs of the photoabsorption decomposition of $C_8H_9OH^-$ and $C_8H_9NH_2^-$ at different resonance energies are shown in Fig. 6. Figure 6(a) shows that at the resonance energy corresponding to the $C_8H_9OH^-$ maximum absorption peak (3.77 eV), a large difference in the KS contribution is observed compared to the neutral molecule [Fig. 2(c), $\omega =$ 3.88 eV]. Two strong positive contributions are found in the region below the resonance energy (dashed black and red circles), suggesting that charge doping changes the charge transition within the C_8H_9OH molecule and the KS contribution. Similar to the neutral monomolecules, the KS contributions of the charge doped $C_8H_9NH_2^-$ [see Fig. 6(b)] and $C_8H_9OH^-$ are in good agreement, indicating that the properties of the monomolecules with two different electron-donating groups do not change significantly after charge doping (see photoabsorption spectrum and PI).

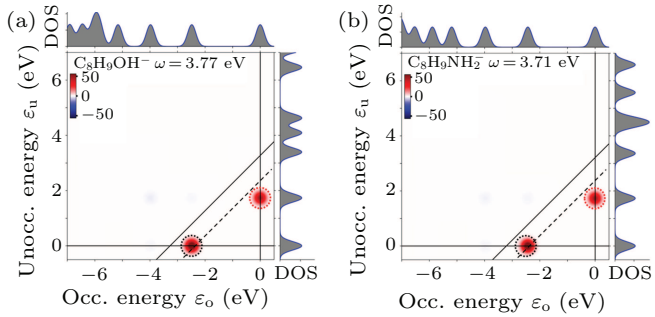


Fig. 6. The TCMs of the photoabsorption decomposition of (a) $C_8H_9OH^-$ and (b) $C_8H_9NH_2^-$ at resonance energies ω. The solid line is the constant for transition energy ($\varepsilon_u - \varepsilon_o = \omega$).

Figure 7 shows the hybridization diagram, PI (see Table S2 in the supporting information), charge transition isosurface and LR-TDDFT photoabsorption spectrum of the HT configuration with negative charge doping based on linear response. Meanwhile, the induced charge density and RT-TDDFT photoabsorption spectrum are shown based on the real-time method. In the HT^{2-} configuration, the negative charge significantly changes the photoabsorption spectrum and PI (compared to the HT configuration in Fig. 3 without charge doping), and the absorption spectrum clearly splits into two peaks. The larger one is located around 1.58 eV and a small peak is generated around 3.70 eV in the high-energy region. The PI of the i excitation mode is also large. The charge density isosurface (in Fig. 7) indicates that the i, ii and iii excitation modes of the charge doped HT^{2-} configuration are the result of the hybridization, which causes the energy level to split between the negatively charged $C_8H_9NH_2^-$ and $C_8H_9OH^-$ molecules [the energy level splitting diagram can be seen in Fig. S6(c)]. The hybridization levels and surface charges demonstrate that the plasmon hybridization phenomenon is more pronounced and simpler in this electron-doped system than in the original molecule. Negative charge doping causes the energy level of the low-energy region to split, which is confirmed by the RT-TDDFT results in the lower panel of Fig. 7. The induced charge density shows clear bonding and anti-bonding modes and is highly consistent with the linear response results. For the HH^{2-} configuration (see Fig. S4), the photoabsorption spectrum does not show double absorption peaks like the HT^{2-} configuration, instead a broad strong absorption peak is formed, the results obtained by RT-TDDFT are consistent with this [see Fig. S5(a)]. From the transition density, it can be seen that the HH^{2-} configuration also forms three plasmon excitation modes (the corresponding plasmon index can be found in Table S2). Similar to the neutral HH configuration, the high-energy mode iii for HH^{2-} configuration (3.62 eV, $S_0 \rightarrow S_{11}$) corresponds to symmetric coupling (anti-bonding), and the low-energy modes i (3.30 eV, $S_0 \rightarrow S_8$) and ii (3.37 eV, $S_0 \rightarrow S_9$) correspond to antisymmetric coupling (bonding), and the energy level splitting diagram can be seen in Fig. S6(d).

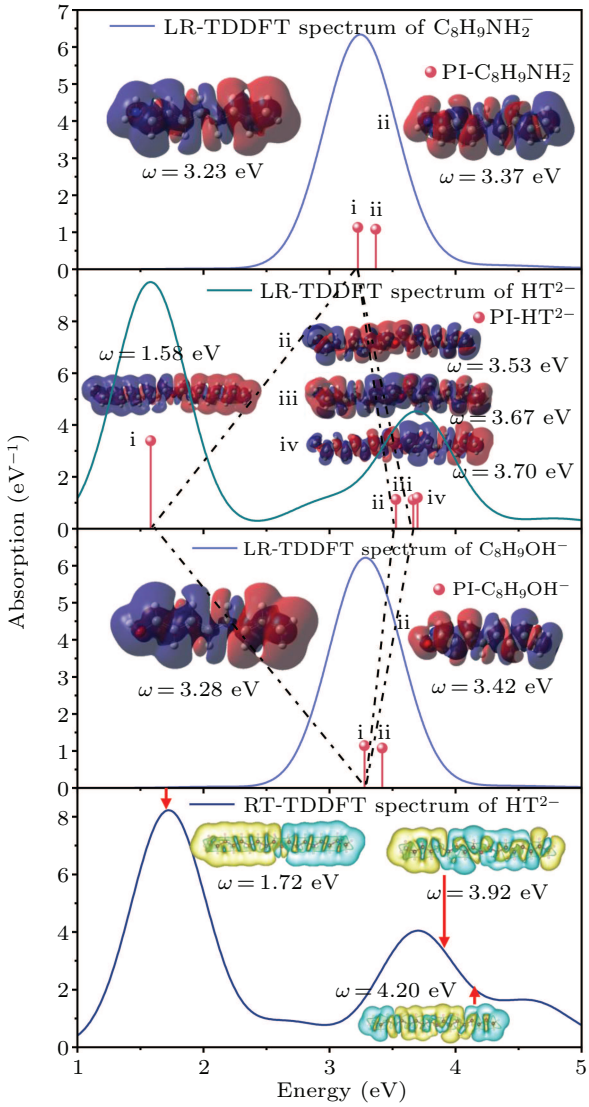


Fig. 7. Schematic diagram of plasmon hybridization for the HT^{2-} configuration, depicting the transition density isosurfaces of the main excitations modes (the vertical red line indicates the PI). The lower panel is the RT-TDDFT photoabsorption spectrum of the HT^{2-} configuration (curve), and the main resonances are shown as the induced density isosurfaces.

The TCMs of the HT^{2-} configuration with negative charge doping is depicted in Fig. 8. Unlike the neutral HT configuration [see Figs. 4(a)–4(d)], the electron–hole contribution

of the doped HT^{2-} configuration is relatively dispersed. The plasmon excitation mode with a resonance energy of 1.72 eV shows a strong positive contribution [see Fig. 8(a)] compared with other resonance energies, and the stronger electronic transition contribution may be the reason why the HT^{2-} configuration produces larger absorption peaks and PI in the lower energy region [see Fig. 8(a) and Table S2]. The positive contributions at the resonance energy of 3.92 eV [dashed black ellipse and dashed red circles in Fig. 8(b)] show a good agreement with the positive contributions of the individual $C_8H_9OH^-$ and $C_8H_9NH_2^-$ [see Figs. 6(a) and 6(b) black and red dashed circles]. This result indicates that the charge transition and electron–hole contribution of the original charged molecule are maintained in the doped HT^{2-} configuration. This response is similar to the traditional hybridization of two different plasmonic objects (i.e., Au and Ag spheres). When neighboring plasmonic particles interact with each other, their plasmon energies mix and split into new modes with shifted energies, and the original properties of individual particle is still retained. A similar phenomenon is observed at higher resonance energies (4.20 eV) [see Fig. 8(c)]. It is worth mentioning that the KS contributions at all three resonance energies produce an additional positive contribution that gradually decreases with the increasing resonance frequency (red solid circle). The possible reason is a new charge transition after $C_8H_9OH^-$ and $C_8H_9NH_2^-$ hybridization and the accompanying split of the new plasmon excitation mode. The TCM of the HH^{2-} configuration [see Figs. S5(b) and S5(c)] shows a phenomenon similar to the HT^{2-} configuration, i.e., the charge transition of the original molecule remains the same.

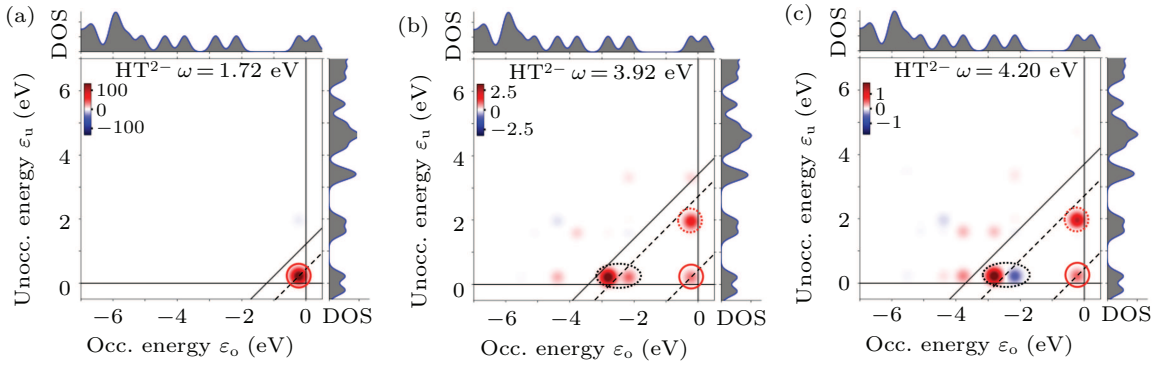


Fig. 8. The TCMs of the photoabsorption decomposition of the HT^{2-} configuration at different resonance energies ω. The solid line is the constant for transition energy ($\varepsilon_u - \varepsilon_o = \omega$).

A comparison of the hybridization of the octatetraene molecules with and without charge doping indicates that the PI of the molecule plasmons is much higher in the charged than the uncharged molecules, and the hybridization phenomenon is more pronounced. Plasmon oscillations are mixed with single particle excitations in the uncharged system because the electrons are more confined. The hybridization is simpler in the HT and HH configurations since there are substantial differences in the molecules when they are combined. In the charged molecules, the extra electrons are not confined to a bond of two atoms, and it will cruise in the whole molecule, coupling electrons in different atoms, which tends to make the excitations in-phase. The in-phase oscillation is similar to the coupled oscillators. Therefore, the PI of the molecules is larger. When the molecules are coupled, the doped cruise electrons will bear more for the plasmon oscillation, and the system retains more of the properties of the individual molecules. In the HT configuration, the same molecular orientation results in easier bonding, leading to the strongest peak. In the HH configuration, the head-to-head orientation makes the antibonding mode much stronger.

Our results indicate that electron doping of molecular plasmonic devices shows promise because it can be used to tune the plasmon mode while retaining the molecules' original properties. It is worth mentioning that molecular plasmons have been used in electrochromic devices, and the generation and annihilation of plasmon excitation can be controlled by charge regulation.[18,19,54] Employing molecular plasmon hybridization, the emission wavelength of the molecular plasmon electrochromic devices can be easily tuned. This effectively economizes the large cost of searching for molecules with certain emission wavelength. Moreover, dynamic tunable electrochromic devices can also be developed by molecular plasmon hybridization, which will greatly expand their applications. Our study here also confirms the effect of charge regulation on plasmon excitation and hybridization properties. Our study helps to provide innovative inspiration for experimental research. Based on the similar phenomenon of plasmon energy splittings and shifts with traditional hybridization of metal nanostructures, molecular plasmonic hybridization is expected to be observed experimentally via carefully analysis of ultrasensitive optical spectra.

4. Conclusion

In summary, we have investigated plasmon hybridization in small molecular systems. The plasmon excitation modes of $C_8H_9NH_2$ and C_8H_9OH molecules are analyzed and identified with the 1D finite electron gas model and PI. Then, we analyze two hybrid configurations (HT and HH) of the two molecules. The PI, the isosurface of the charge transition den-

sity, the induced charge density and TCM analysis show that the HT configuration without charge doping can produce a hybridization result better than the other two configurations. The possible reason is that the two electron-donating groups (–OH and $–NH_2$) are in alignment, resulting in co-bond effect. Finally, we evaluate the effect of charge doping on plasmon excitation and hybridization properties. The largest effect is observed on the absorption spectrum of the HH configuration, which exhibits a strong absorption peak, a large change in the PI, and pronounced hybridization with energy level splitting. Plasmon hybridization occurs preferably on molecular groups with strong conjugated electron-donating groups, and charge doping substantially changes the molecular plasmon excitation and hybridization. These results provide a basis for in-depth research on MPH and the development of related applications.

Acknowledgements

Project supported by the National Natural Science Foundation of China (Grant Nos. 12274054 and 12074054), and the Fundamental Research Funds for the Central Universities (Grant No. DUT21LK06).

References

[1] Novotny L and Hecht B 2012 *Principles of Nano-Optics* (Cambridge: Cambridge University Press)
[2] Kazuma E, Jung J, Ueba H, Trenary M and Kim Y 2018 *Science* **360** 521
[3] Chu W, Saidi W A and Prezhdo O V 2020 *ACS Nano* **14** 10608
[4] Zhang X, Li X, Reish M E, Zhang D, Su N Q, Gutierrez Y, Moreno F, Yang W, Everitt H O and Liu J 2018 *Nano Lett.* **18** 1714
[5] Li X, Xiao D and Zhang Z 2013 *New J. Phys.* **15** 023011
[6] Tame M S, McEnery K, Özdemir Ş, Lee J, Maier S A and Kim M 2013 *Nat. Phys.* **9** 329
[7] Rossi T P, Shegai T, Erhart P and Antosiewicz T J 2019 *Nat. Commun.* **10** 3336
[8] Rossi T P, Kuisma M, Puska M J, Nieminen R M and Erhart P 2017 *J. Chem. Theory Comput.* **13** 4779
[9] Schira R and Rabilloud F 2019 *J. Phys. Chem. C* **123** 6205
[10] Conley K M, Nayyar N, Rossi T P, Kuisma M, Turkowski V, Puska M J and Rahman T S 2019 *ACS Nano* **13** 5344
[11] Della Sala F, Pezzolla M, D'Agostino S and Fabiano E 2019 *ACS Photon.* **6** 1474
[12] Yan J, Yuan Z and Gao S 2007 *Phys. Rev. Lett.* **98** 216602
[13] Bernadotte S, Evers F and Jacob C R 2013 *J. Phys. Chem. C* **117** 1863
[14] Bursi L, Calzolari A, Corni S and Molinari E 2016 *ACS Photon.* **3** 520
[15] Krauter C M, Schirmer J, Jacob C R, Pernpointner M and Dreuw A 2014 *J. Chem. Phys.* **141** 104101
[16] Krauter C M, Bernadotte S, Jacob C R, Pernpointner M and Dreuw A 2015 *J. Phys. Chem. C* **119** 24564
[17] Zhang K, Wang H and Fang M 2019 *Chem. Phys. Lett.* **721** 38
[18] Lauchner A, Schlather A E, Manjavacas A, Cui Y, McClain M J, Stec G J, Garcia de Abajo F J, Nordlander P and Halas N J 2015 *Nano Lett.* **15** 6208
[19] Stec G J, Lauchner A, Cui Y, Nordlander P and Halas N J 2017 *ACS Nano* **11** 3254
[20] Zhang R, Bursi L, Cox J D, Cui Y, Krauter C M, Alabastri A, Manjavacas A, Calzolari A, Corni S, Molinari E, Carter E A, Garcia de Abajo F J, Zhang H and Nordlander P 2017 *ACS Nano* **11** 7321
[21] Manjavacas A, Marchesin F, Thongrattanasiri S, Koval P, Nordlander P, Sanchez-Portal D and García de Abajo F J 2013 *ACS Nano* **7** 3635
[22] Zeng S, Baillargeat D, Ho H P and Yong K T 2014 *Chem. Soc. Rev.* **43** 3426
[23] Zhang R, Zhang Y, Dong Z, Jiang S, Zhang C, Chen L, Zhang L, Liao Y, Aizpurua J and Luo Y E 2013 *Nature* **498** 82
[24] Moskovits M 2005 *J. Raman Spectrosc.* **36** 485
[25] Neubrech F, Huck C, Weber K, Pucci A and Giessen H 2017 *Chem. Rev.* **117** 5110
[26] Anker J N, Hall W P, Lyandres O, Shah N C, Zhao J and Van Duyne R P 2008 *Nat. Mater.* **7** 442
[27] Oulton R F, Sorger V J, Genov D, Pile D and Zhang X 2008 *Nat. Photon.* **2** 496
[28] Cushing S K, Li J, Meng F, Senty T R, Suri S, Zhi M, Li M, Bristow A D and Wu N 2012 *J. Am. Chem. Soc.* **134** 15033
[29] Linic S, Christopher P and Ingram D B 2011 *Nat. Mater.* **10** 911
[30] Fang Y and Sun M 2015 *Light Sci. Appl.* **4** e294
[31] Memmi H, Benson O, Sadofev S and Kalusniak S 2017 *Phys. Rev. Lett.* **118** 126802
[32] Dintinger J, Klein S, Bustos F, Barnes W L and Ebbesen T W 2005 *Phys. Rev. B* **71** 035424
[33] Cui Y, Lauchner A, Manjavacas A, Abajo F J G D, Halas N J and Nordlander P 2016 *Nano Lett.* **16** 6390
[34] Prodan E and Nordlander P 2004 *J. Chem. Phys.* **120** 5444
[35] Gil-Guerrero S, Peña-Gallego Á and Mandado M 2019 *J. Phys. Chem. C* **124** 1585
[36] Frisch M, Trucks G, Schlegel H, *et al.* 2016 *Gaussian 16* (Gaussian, Inc. Wallingford, CT)
[37] Becke A D 1988 *Phys. Rev. A* **38** 3098
[38] Parr R G 1980 *Horizons of Quantum Chemistry* (Berlin: Springer) pp. 5–15
[39] Yanai T, Tew D P and Handy N C 2004 *Chem. Phys. Lett.* **393** 51
[40] Perdew J P, Burke K and Ernzerhof M 1996 *Phys. Rev. Lett.* **77** 3865
[41] Yabana K and Bertsch G 1996 *Phys. Rev. B* **54** 4484
[42] Blöchl P E 1994 *Phys. Rev. B* **50** 17953
[43] Rossi T P, Lehtola S, Sakko A, Puska M J and Nieminen R M 2015 *J. Chem. Phys.* **142** 094114
[44] Mortensen J J, Hansen L B and Jacobsen K W 2005 *Phys. Rev. B* **71** 035109
[45] Enkovaara J, Rostgaard C, Mortensen J J, *et al.* 2010 *J. Phys.: Condens. Matter* **22** 253202
[46] Larsen A H, Vanin M, Mortensen J J, Thygesen K S and Jacobsen K W 2009 *Phys. Rev. B* **80** 195112
[47] Kuisma M, Sakko A, Rossi T P, Larsen A H, Enkovaara J, Lehtovaara L and Rantala T T 2015 *Phys. Rev. B* **91** 115431
[48] Larsen A H, Mortensen J J, Blomqvist J, Castelli I E, Christensen R, Dułak M, Friis J, Groves M N, Hammer B and Hargus C 2017 *J. Phys.: Condens. Matter* **29** 273002
[49] Harris C R, Millman K J, Van Der Walt S J, Gommers R, Virtanen P, Cournapeau D, Wieser E, Taylor J, Berg S and Smith N J 2020 *Nature* **585** 357
[50] Virtanen P, Gommers R, Oliphant T E, Haberland M, Reddy T, Cournapeau D, Burovski E, Peterson P, Weckesser W and Bright J 2020 *Nat. Methods* **17** 261
[51] Hunter J D 2007 *Comput. Sci. Eng.* **9** 90
[52] Malola S, Lehtovaara L, Enkovaara J and Hakkinen H 2013 *Acs Nano* **7** 10263
[53] Kuisma M, Rousseaux B, Czajkowski K M, Rossi T P, Shegai T, Erhart P and Antosiewicz T J 2022 *ACS Photon.* **9** 1065
[54] Zhang H, Ming S, Liang Y, Feng L, Talin A and Xu T 2019 *ACS Appl. Mater. Inter.* **11** 20581